Applications in Energy and Combustion Science 27 (2026) 100542

Contents lists available at ScienceDirect

Applications in Energy and Combustion Science

journal homepage: www.elsevier.com/locate/jaecs

Numerical study of forced ignition and minimum ignition energy of difluoromethane (R32)/air mixtures

Chunwei Wu [a,*], Nafi Farzana [b], Heejeong Kim [a], Bo Shu [b], Ulrich Maas [a], Chunkan Yu [a]

[a] Institute of Technical Thermodynamics, Karlsruhe Institute of Technology, Karlsruhe, Germany
[b] Physikalisch-Technische Bundesanstalt, Braunschweig, Germany

ARTICLE INFO

Keywords:
Forced ignition
Minimum ignition energy
Flame kernel formation
Fluorinated refrigerants
R32

ABSTRACT

Difluoromethane (R32) is a mildly flammable refrigerant widely adopted in low-GWP air-conditioning systems. Understanding its forced ignition characteristics is essential for assessing safety risks associated with accidental ignition. In this study, the forced ignition behavior of stoichiometric R32/air mixtures is investigated numerically using the in-house code INSFLA, which solves one-dimensional conservation equations with detailed molecular transport and a newly developed skeletal CH_2F_2 kinetic mechanism. The mechanism, derived from an optimized detailed model, includes 39 species and 75 reactions and accurately reproduces the key fluorine-abstraction and chain-branching pathways governing R32 oxidation. The effects of ignition energy, ignition radius, ignition duration, and geometry on flame-kernel formation, quenching, and propagation are examined. Localized ignition may occur at moderate energies but often quenches; and only sufficiently high energies produce self-sustained flames. The minimum ignition energy for a successful flame propagation, MIE_{prop}, scales approximately with r_s^3 for large ignition radii but becomes nearly constant for small r_s. Combustion of R32 produces substantial amounts of HF, which becomes a dominant reaction product during sustained propagation. These findings provide mechanistic insight into R32 ignition behavior and safety implications for mildly flammable refrigerants.

1. Introduction

The refrigerant difluoromethane CH_2F_2, also known as R32, is widely regarded as one of the most balanced refrigerants concerning environmental impact, energy efficiency, safety, and cost-effectiveness [1]. It is a type of hydrofluorocarbon (HFC) refrigerant that has gained popularity in recent years due to its zero ozone depletion potential (ODP) and relatively low global warming potential (GWP = 675), around three times lower compared to other commonly used refrigerants like R410 A with GWP of 2088 [2,3], according to the international standard *ISO 817:2014 Refrigerants - Designation and safety classification* [4]. Since safety and environmental issues are crucial when dealing with refrigerants [5,6], the explosion characteristics of R32 refrigerant and the emission of toxic products are of great interest.

Various studies reported experimental investigations of R32. including its burning velocities [7], possible ignition and flame propagation by alternating current (AC) electric sparks as an ignition source [8], and quenching distances [9]. Regarding risk assessment, an experimental investigation on the main toxic combustion product, hydrogen fluoride (HF), of R32 was conducted in [10].

In addition, various efforts have been made to understand the combustion properties of R32 in more detail based on numerical simulations. In [11] a detailed chemical kinetic model for R32/air mixtures was developed and validated against experimental measurements of flammability and laminar burning velocities. Several reactions that make the most significant contributions to the laminar burning velocity were determined, e.g. uni-molecular decomposition reaction $CH_2F_2 \rightarrow CHF+HF$ and oxidation step $CHF_2+O_2 \rightarrow CF_2O+OH$. In [2] some combustion properties, such as adiabatic flame temperatures, laminar burning velocities, and combustion products of R32 under various conditions, are discussed and compared with other commercially used refrigerants, such as 2,3,3,3-tetrafluoropropene (R1234yf) and isobutane (R600a). In [7], spherical flame propagation was studied together with an optically thin radiation model, showing that the effects of stretch and radiation are significant for such low burning velocity flames.

Despite numerous experimental and numerical investigations on the R32 refrigerant, there are still few studies reporting on its ignition by sparks. For instance, Askar et al. [12] measured the minimum ignition energy of R32/air mixtures using a spark igniter and found

* Corresponding author.
E-mail address: chunwei.wu@kit.edu (C. Wu).

https://doi.org/10.1016/j.jaecs.2026.100542
Received 30 April 2026; Received in revised form 3 July 2026; Accepted 16 July 2026
Available online 25 July 2026

a strong dependence on spark gap and duration. Takizawa et al. [9] further reported that R32 can be ignited by high-energy sparks under near-stoichiometric conditions.

However, the combined effects of ignition energy, geometry, and spark duration on R32 ignition and flame-kernel development remain unclear. Furthermore, previous studies have primarily focused on ignition limits and flame propagation, while little attention has been paid to the formation of toxic decomposition products during ignition attempts.

For a fluorinated refrigerant like R32, localized energy deposition may induce chemical decomposition even when a self-sustained flame is not established, potentially resulting in HF formation. The occurrence and safety implications of such events remain largely unexplored.

The present study addresses this gap through detailed one-dimensional simulations to clarify the effects of energy deposition characteristics on ignition behavior in R32/air mixtures. Particular attention is paid not only to the minimum ignition energy and flame-kernel evolution but also to HF formation under both successful and unsuccessful ignition conditions, providing new insights into the fire and toxicological hazards associated with accidental R32 releases.

2. Skeletal chemical kinetic model for CH_2F_2 oxidation

The chemical kinetic model used in the present forced-ignition simulations is based on an optimized detailed CH_2F_2 oxidation mechanism developed in our previous work [13]. The parent mechanism combines a dedicated fluorinated reaction subset with a small-molecule hydrocarbon oxidation core. The fluorinated chemistry, including fuel decomposition, abstraction reactions, fluorinated-radical oxidation, and HF-forming pathways, was primarily adopted from the NIST fluorocarbon database [14]. Compared with earlier formulations relying on GRI-Mech 3.0, the present mechanism uses the C_0–C_2 hydrocarbon chemistry from NUIG Mech 1.3 [15], which provides a more extensively validated description of the H/O/C chemistry relevant to small-molecule oxidation.

In the parent mechanism, optimization was restricted to selected reactions involving fluorinated species, while the hydrocarbon core was retained from the validated base model. This approach was chosen to improve the description of CH_2F_2 oxidation without compromising the consistency of the underlying H/O/C reaction system. The optimized detailed mechanism was previously validated against experimental ignition delay times and laminar burning velocities, showing improved agreement relative to earlier literature models [13].

For the present work, a skeletal version of the optimized mechanism was developed to reduce the computational cost of the one-dimensional forced-ignition simulations. This reduction was necessary because the simulations include detailed transport, transient heat release, and systematic variation of ignition parameters. The skeletal mechanism was generated using sensitivity analyses of ignition delay time and laminar burning velocity as the principal reduction targets. During reduction, particular attention was given to retaining the chemistry controlling ignition-kernel formation, extinction, and early flame propagation under stoichiometric CH_2F_2/air conditions. Therefore, the reduced mechanism preserves the dominant pathways for fuel consumption, radical-pool buildup, heat release, and HF formation, which directly influence whether a locally ignited kernel develops into a self-sustained flame or is quenched by diffusive losses.

The final skeletal mechanism contains 39 species and 75 elementary reactions. It retains the main reaction classes relevant to CH_2F_2 oxidation, including unimolecular fuel decomposition, abstraction reactions forming CHF_2, oxidation of fluorinated radicals by O_2 and other small reactive species, formation of stable fluorinated intermediates, and HF-producing pathways. The key H/O branching and propagation reactions are also retained to capture the competition between chemical heat release and diffusive heat loss during ignition-kernel development.

The performance of the skeletal mechanism was evaluated against the validation targets used during mechanism development. To directly assess the effect of reduction, predictions from the detailed parent mechanism are also included in Figs. 1 and 2 together with the skeletal-mechanism predictions. The parent mechanism was originally developed for CH_2F_2, CH_4, and CH_2F_2/CH_4 blend oxidation chemistry; therefore, the present pure-CH_2F_2 validation provides a direct check that the skeletal mechanism preserves the CH_2F_2-specific ignition and flame-propagation behavior of the parent model. The ignition-delay validation in Fig. 1 uses the stoichiometric CH_2F_2/oxidizer data reported by Farzana et al. [13] under 95% dilution, while the laminar-burning-velocity validation in Fig. 2 uses the pure CH_2F_2/air data reported by Hesse et al. [16]. Good agreement was obtained for the principal reactivity trends, particularly ignition delay times and laminar burning velocities, indicating that the skeletal model retains the dominant kinetic features required for reliable prediction of ignition, quenching, and early flame propagation under the conditions considered in this work.

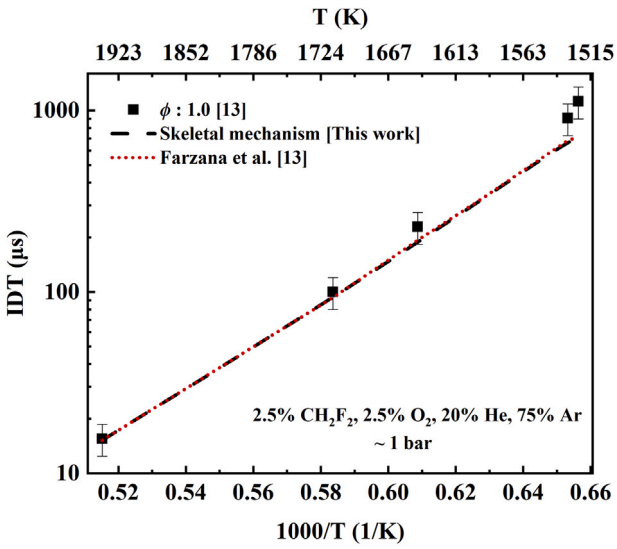

Fig. 1. Ignition delay times of stoichiometric ($\phi = 1$) CH_2F_2/oxidizer mixtures under 95% dilution at $P_5 = 1$ bar. Symbols denote experimental data from Farzana et al. [13]; lines show predictions from the skeletal mechanism and the detailed parent mechanism.

For the flame-speed comparison, the plotted symbols correspond specifically to the radiation-corrected optically thin model (OTM) unstretched laminar burning velocities reported for $X_{yf} = 0$. These corrected values were used because the present flame-speed simulations are adiabatic, freely propagating, and unstretched, while radiation heat losses are not negligible for the relatively slow CH_2F_2/air flames. Uncertainty bars were added to the experimental symbols; the flame-speed uncertainty is approximately ± 0.4 cm s^{-1}, while the measured IDTs are shown with a $\pm 20\%$ variation band and a temperature uncertainty factor of 1.018.

To assess numerical reproducibility, the mechanism development and validation calculations were carried out using the PTB simulation framework. In addition, a representative flame-speed case at $\phi = 1$ was independently reproduced using an in-house simulation tool developed at KIT-ITT. The two implementations showed excellent agreement for this test case. Details of the KIT-ITT methodology are provided in Section 3.

3. Simulation methodology

The in-house code INSFLA [17] at KIT-ITT is used to model the induced ignition process of CH_2F_2/air mixtures. This code numerically solves the conservation equations for total mass, species mass, momentum, and energy in a one-dimensional configuration, accounting for

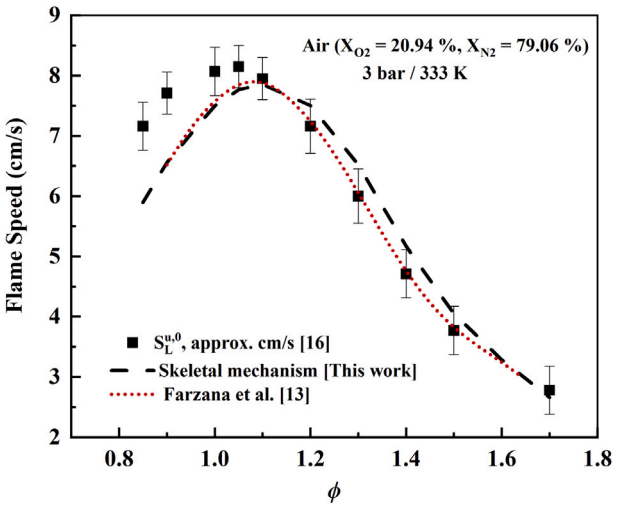

Fig. 2. Laminar burning velocity of CH_2F_2/air at $p_0 = 3$ bar and $T_0 = 333$ K. Symbols denote radiation-corrected optically thin model unstretched laminar burning velocities for pure CH_2F_2/air from Hesse et al. [16]; Lines show predictions from the skeletal mechanism and the detailed parent mechanism.

detailed chemical kinetics and detailed molecular transport phenomena, including thermal diffusion. The computational scheme employs adaptive spatial discretization and time-stepping, with the latter governed by an error-control algorithm. The outcome of the simulations are spatio-temporal profiles of pressure, temperature and chemical composition during ignition and early flame propagation process. Although this one-dimensional laminar framework does not capture multidimensional effects or ignition kernel distortions in practical systems, it is well suited for investigating the fundamental chemical and diffusive mechanisms governing forced ignition and MIE scaling. The greatly reduced computational cost compared to higher-dimensional simulations also makes systematic parametric studies practical.

A transformation into mass-based Lagrangian coordinate Ψ is used in simulations with [17,18]

$$\frac{\partial r}{\partial \Psi} - \frac{1}{\rho r^{\alpha}} = 0$$

where α is the geometry-dependent parameter. For an infinite slab, $\alpha = 0$; for infinite cylinder, $\alpha = 1$; for a sphere, $\alpha = 2$. This coordinate transformation eliminates convective terms and also allows flame propagation driven by chemical reactions to be distinguished from thermal expansion induced by the high-temperature ignition kernel.

The initial conditions for the simulations corresponds to a premixed, homogeneous, stoichiometric ($\phi = 1$) CH_2F_2/air mixture with an initial temperature of $T_0 = 298$ K. The present study focuses on the stoichiometric R32/air mixture because it represents a condition of practical interest and provides a suitable reference state for investigating ignition behavior. Extension to lean and rich mixtures will be considered in future work. The skeletal chemical kinetic model for CH_2F_2 oxidation can be found in Section 2. All simulations are performed under the assumption of constant pressure, $p = 1$ bar, which is a reasonable approximation for the ignition duration used in this study [17].

For flames with curved geometries, extinction may occur even after a successful flame kernel formation. This behavior can be interpreted through the curvature-induced modification of the diffusion term in the species conservation equation [17]:

$$\frac{1}{r^{\alpha}} \frac{\partial}{\partial r} \left(r^{\alpha} j_i \right) = \frac{\partial j_i}{\partial r} + \frac{\alpha}{r} j_i, \tag{1}$$

where j_i denotes the diffusion flux of species i, r is the radial coordinate, and α is a geometry-dependent parameter.

For the planar configuration, $\alpha = 0$, and the curvature-related contribution vanishes. In contrast, for curved geometries ($\alpha > 0$), the additional term $\frac{\alpha}{r} j_i$ introduces an enhanced diffusive transport compared to the planar case under the same local conditions of j_i and r.

For R32, where the overall chemical reactivity is relatively weak, this curvature-enhanced diffusion can significantly influence the early flame development stage. This effect is particularly pronounced at small flame radii, where r is small and the effective curvature term α/r becomes large, leading to intensified diffusive losses of heat and active species and thereby promoting flame weakening or eventual extinction.

To investigate the effect of curvature on ignition and early flame propagation, one-dimensional spherical and cylindrical configurations are performed. A schematic of the induced ignition with one-dimensional geometries is shown in Fig. 3 Neumann boundary conditions are applied to temperature and all species at both the inner and outer boundaries, ensuring a symmetry condition at the center and a non-catalytic, adiabatic condition at the outer boundary. The initial and boundary conditions are summarized in Table 1

Starting from $t = 0$, a time- and space-dependent external source term $\dot{q} = \dot{q}(r,t)$ is applied to the conservation equations at the center of the computational domain. The power density $\dot{q}$ follows an exponential spatial distribution and remains constant throughout the ignition period, which produces a near-rectangular profile while guaranteeing a smooth and differentiable behavior [17]:

$$\begin{aligned} \dot{q} &= \dot{q}_{\max} e^{-\left(\frac{r}{r_s}\right)^8} \quad \text{for} \quad 0 < t \le \tau_s \\ \dot{q} &= 0 \quad \text{for} \quad t > \tau_s \end{aligned} \tag{2}$$

Table 1
Initial and boundary conditions used in the one-dimensional simulations.

Location	Variable	Condition
Initial condition	Species mass fractions Y_i	Homogeneous mixture of CH_2F_2/air, $\phi = 1$
$t = 0$	Temperature T	$T = T_0 = 298$ K
	Pressure p	$p = p_0 = 1$ bar
Inner boundary	Radial coordinate r	$r = 0$
(symmetry center)	Species mass fractions Y_i	$\frac{\partial Y_i}{\partial \psi} = 0$
$\psi = 0$	Temperature T	$\frac{\partial T}{\partial \psi} = 0$
	Pressure p	$\frac{\partial p}{\partial \psi} = 0$
Outer boundary	Radial coordinate r	$r = r_{out}$
(non-catalytic, adiabatic)	Species mass fractions Y_i	$\frac{\partial Y_i}{\partial \psi} = 0$
$\psi = \psi_{out}$	Temperature T	$\frac{\partial T}{\partial \psi} = 0$
	Pressure p	$\frac{\partial p}{\partial \psi} = 0$

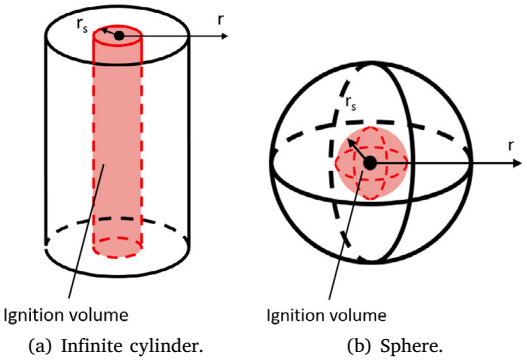

Fig. 3. Schematic of the induced ignition with one-dimensional geometries in quiescent mixture.

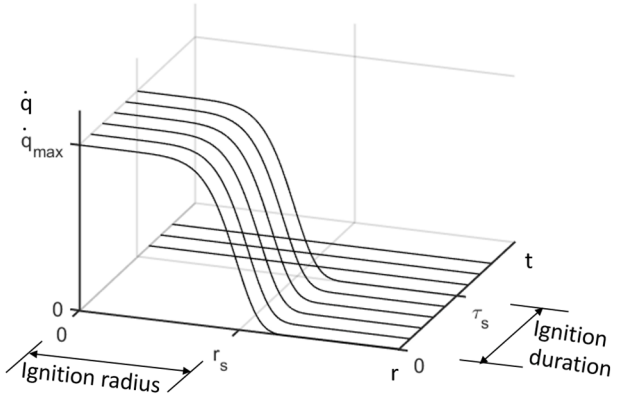

Fig. 4. Temporal–spatial profile of the ignition energy density [19].

where r_s represents the ignition radius and τ_s represents the ignition duration. In this study, different ignition duration (τ_s ranging from 10^{-4} to 10^{-2} s), and different ignition radii (r_s ranging from 1 to 10 mm) are systematically varied to investigate their effects on the minimum ignition energy, including the influence of ignition volume and curvature. After the specified spark duration, the external energy input is terminated. Fig. 4 shows the ignition energy density distribution.

The total deposited energy is obtained by integrating the power density over both space and time.

For spherical geometry, the ignition energy E_{ig} has units of J.

$$E_{ig} = \int_0^{\infty} \int_0^{\tau_s} 4\pi r^2 \dot{q} dr dt \tag{3}$$

The maximal ignition energy density q_{max}, which is $\dot{q}_{\max}$ times ignition duration τ_s, is

$$q_{max} = \dot{q}_{\max} \cdot \tau_s = 0.886 \frac{E_{ig}}{\frac{4}{3}\pi r_s^3}. \tag{4}$$

For an infinite cylinder, the ignition energy E_{ig} is expressed in terms of energy per unit length, with the unit of J/m.

$$E_{ig} = \int_0^{r_s} \int_0^{\tau_s} 2\pi r \dot{q} dr dt \tag{5}$$

The maximal ignition energy density q_{max}, which is $\dot{q}_{\max}$ times ignition duration τ_s, is

$$q_{max} = \dot{q}_{\max} \cdot \tau_s = 0.906 \frac{E_{ig}}{\pi r_s^2}. \tag{6}$$

The factor 0.886 and 0.906 result from integrating the exponential function $e^{-(r/r_s)^8}$ over the spherical or cylindrical domain $[0, \infty]$.

In this study, the model of the external ignition energy is not designed to reproduce a specific experimental set-up, but to investigate the qualitative influences of ignition radius, duration and geometry on ignition and HF emission events, which are also observed in experiments.

4. Results and discussions

4.1. Flame scenarios

Starting from $t = 0$, ignition energy is deposited within the ignition volume, leading to heating of the fresh mixture. At the end of the ignition duration ($t = \tau_s$), the external energy input is terminated. Three qualitatively different ignition scenarios are observed:

- Scenario I: ignition failure
- Scenario II: successful ignition followed by flame extinction
- Scenario III: self-sustained flame

Fig. 5 illustrates the spatio-temporal evolution of HF mass fraction for the three scenarios. The HF mass fraction, rather than temperature, is used to distinguish between these scenarios, as significant HF production occurs only during flame kernel formation, whereas temperature increases may also result from external energy deposition.

For the ignition failure scenario, the maximum HF mass fraction observed after the application of the external energy source is approximately three orders of magnitude lower than that in cases where a flame kernel is successfully established. This qualitative difference indicates that, within the ignition region, the mixture is only heated. In other words, the supplied energy mainly increases the local temperature without triggering fast chemical reactions. Once the external energy input is terminated, the temperature rapidly decreases due to heat losses and the absence of exothermic reactions. Consequently, no ignition event occurs, as ignition is associated with accelerated chemical kinetics and substantial heat release, neither of which is present in this case.

In contrast, the flame extinction scenario exhibits a different behavior. Immediately following the energy deposition, a local and pronounced increase in HF mass fraction is detected, clearly indicating that chemical reactions are initiated and a flame kernel is formed. However, this initial kernel remains small in size, resulting in a flame front with strong positive curvature. For the R32/air mixtures considered in this study, which are characterized by relatively low heat release rates, the flame is very sensitive to the strong diffusive heat loss through curvature effect. As a result, the flame is unable to sustain itself and eventually quenches. Following extinction, the produced HF gradually diffuses into the surrounding mixture, causing a continuous decrease in the maximum HF mass fraction.

For the flame propagation case, a sustained and intense production of HF is observed after ignition, reflecting fast chemical reactions and successful flame development. Although the maximum HF mass fraction shows an initial decrease after ignition, again due to strong diffusive heat loss caused by large curvature, the situation differs fundamentally from the extinction case. When the excess enthalpy provided by the ignition source is sufficiently high, it compensates for the adverse curvature effects and supports continued reaction progress. This additional energy enables the flame to overcome the curvature effect for low radii, allowing it to grow, stabilize, and ultimately transition into a self-sustained propagating flame.

4.2. Flame kernel formation and subsequent propagation or extinction

To investigate the conditions governing reaction onset and the transition to self-sustained flame propagation, Fig. 6 presents the dependence of the central temperature at $t = 0.1$ s, and the maximum central HF mass fraction on the ignition energy E_{ig}. The formation of HF serves as an indicator of chemical reaction initiation, whereas a high central temperature at $t = 0.1$ s suggests that the reacting kernel persists without quenching. The time $t = 0.1$ s is chosen as the end of the simulation, since the transition to self-sustained flame propagation occurs within $t \approx 0.02$–0.06 s under the investigated conditions. Therefore, if the central temperature remains high at $t = 0.1$ s, the flame can be considered self-sustained and unlikely to quench.

For R32/air mixtures, negligible chemical activity is observed for ignition energies below 2.5 mJ (Scenario I: ignition failure). When the ignition energy exceeds 3.0 mJ, distinct reaction zones can be observed (Scenario II: successful ignition followed by flame extinction). Within the transition range of 2.5–3.0 mJ, increasing E_{ig} enhances the reaction intensity, as reflected by a rise in the peak HF mass fraction. Accordingly, the minimum ignition energy for flame initiation is defined as $MIE_{ini} = 3.0$ mJ, corresponding to the upper bound of this transition regime. Beyond this threshold, the formation of a flame kernel is consistently observed, and the central HF mass fraction approaches a nearly constant value. In comparison, for typical hydrocarbon fuels (e.g., using CO_2 as a reaction marker), the corresponding transition

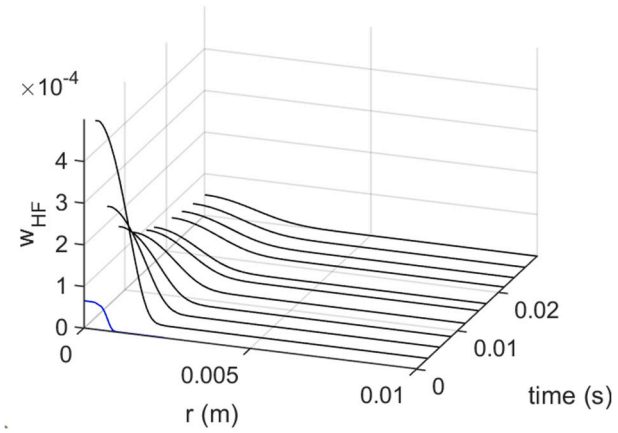

(a) Scenario I.

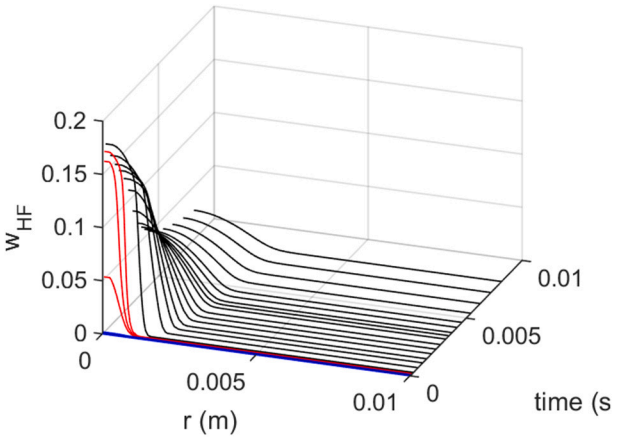

(b) Scenario II.

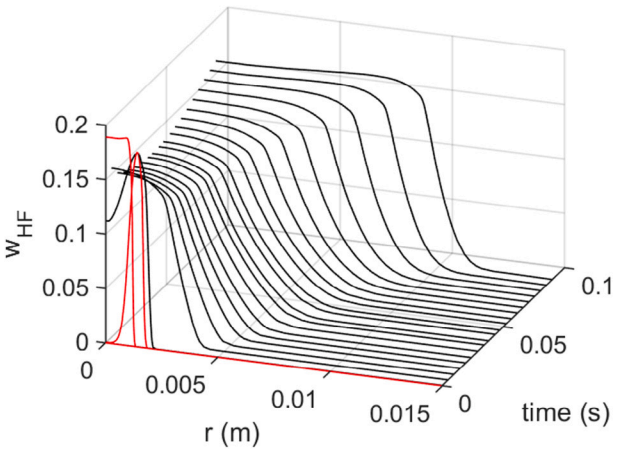

(c) Scenario III.

Fig. 5. Spatio-temporal evolution of HF mass fraction under different scenarios. Blue lines represent HF mass fractions during the spark duration, red lines represent to the ignition phase, and black lines represent the post-ignition stage. In Scenario III (flame propagation), the spark duration is negligible compared to the flame propagation timescale and is therefore not shown.

occurs over a much narrower ignition energy interval of approximately 0.1 mJ [20].

With further increase in ignition energy, once the minimum ignition energy for sustained propagation is reached (MIE_{prop} = 8.6 mJ), the flame becomes self-sustaining and is no longer inhibited by curvature effects (Scenario III).

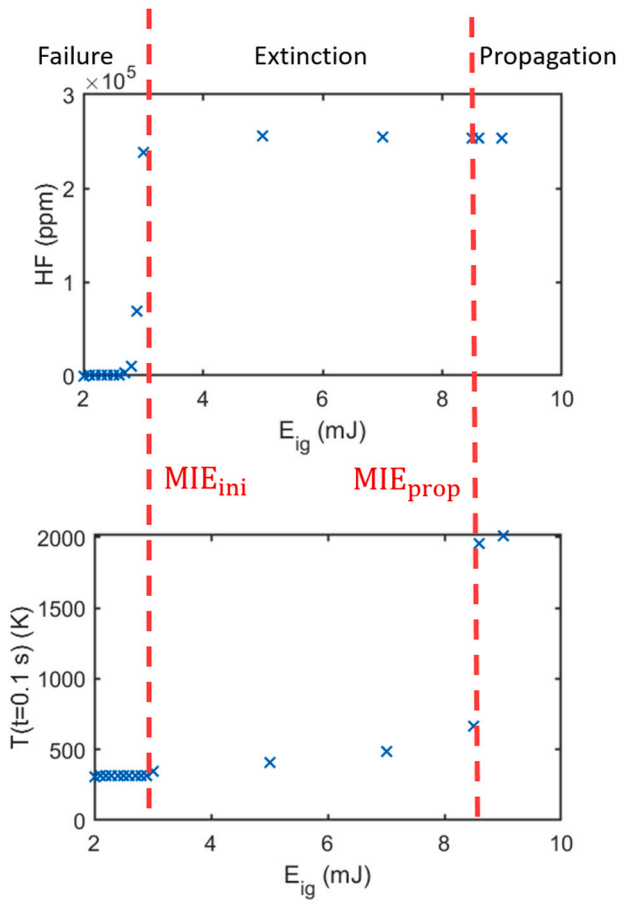

Fig. 6. Dependence of the central temperature at $t = 0.1$ s and the maximum central HF mass fraction on the ignition energy.

In summary, during the spark duration, the R32/air mixture within the ignition volume is primarily heated by the deposited energy. Depending on the magnitude of E_{ig}, this temperature rise may or may not be sufficient to trigger chemical reactions. Even in cases where ignition occurs, the resulting flame kernel may extinguish due to the inherently low reactivity of R32 and strong diffusive effects, causing the central temperature to decay toward ambient conditions. However, when E_{ig} exceeds MIE_{prop}, the additional enthalpy supplied by the spark enables the flame to overcome this critical stage, ultimately leading to stable, self-sustained propagation. In the present study, successful ignition refers to the formation of a localized reacting zone and the initiation of a flame-kernel, whereas self-sustained flame refers to a non-extinguished propagating flame. Note that the MIE calculated in this work may quantitatively differ from the experimentally measured MIE, since three-dimensional effects such as electrode effects are not considered.

4.3. Slow and fast flame

Fig. 7 illustrates the effect of curvature by comparing flame-kernel evolution in spherical and cylindrical geometries. The flame radius is defined at the location of the peak heat release rate.

In the spherical configuration, two quasi-linear propagation phases with different slopes can be clearly identified. These slopes correspond to the flame propagation speed. Shortly after ignition, the flame radius is small, resulting in a large curvature (inversely proportional to the

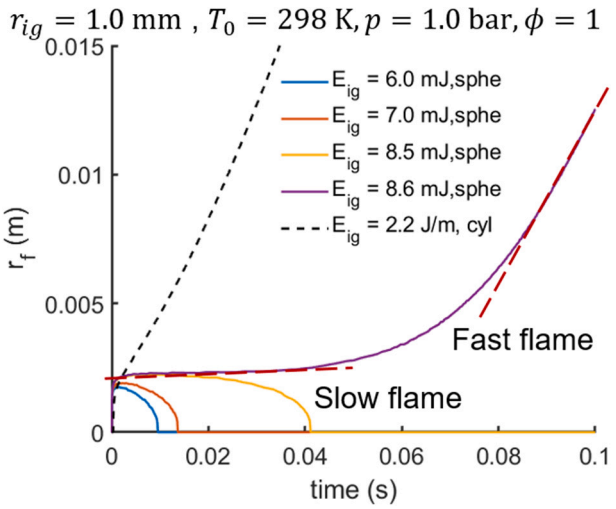

Fig. 7. Evolution of the flame kernel. The flame radius is defined at the location of the peak heat release rate.

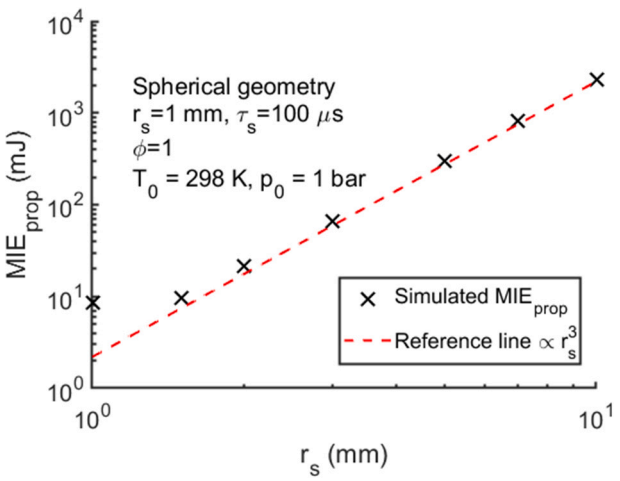

Fig. 8. Dependence of MIE_{prop} on ignition radius.

flame radius) of the flame front. Due to the strong competition between chemical heat release and diffusive heat losses, the flame initially propagates at an extremely low speed (only about 0.2 cm/s) and may quench if the ignition energy is insufficient. As the ignition energy increases, the flame kernel is able to expand further; at $E_{ig} = 8.6$ mJ, it overcomes the critical phase associated with large curvature. Once the flame front moves sufficiently far from the center, such that curvature effects become weak, the propagation speed increases significantly, and the flame develops into a self-sustained propagating regime.

In the cylindrical configuration, the flame curvature is smaller than in the spherical case for the same flame radius; consequently, curvature-induced effects are weakened. Under the same ignition radius and duration as those applied in the spherical geometry, the flame transitions to a fast propagation regime immediately after kernel formation.

In general, the characteristic curvature-induced behavior – namely an initial slow propagation phase, a subsequent acceleration, and possible flame extinction – can still be observed in the cylindrical configuration, but it is expected to occur more readily when a smaller ignition radius is employed.

4.4. Dependence of MIE on ignition radius and ignition duration

The dependence of MIE_{prop} on the ignition radius for spherical geometry is investigated, and the results are presented in Fig. 8.

In the simulations, the ignition radius influences MIE_{prop} in two ways:

- The ignition volume depends on the ignition radius. For spherical geometries, the ignition volume, and consequently the mass of the R32/air mixture within this volume, is proportional to r_s^3. The minimum energy required to heat the mixture to the temperature at which fast chemical reactions occur is therefore also approximately proportional to r_s^3. As shown in Fig. 8, for larger ignition radii ($r_s > 1.5$ mm), MIE_{prop} nearly coincides with the reference line proportional to r_s^3.
- Strong heat losses caused by diffusion associated with flame curvature decrease as the flame radius increases. At small ignition radii, the local flame curvature is high, leading to strong heat losses caused by diffusion and a limited ability of the flame kernel to grow. In this regime, MIE_{prop} remains nearly constant with decreasing r_s, since further reduction in the ignition radius does not significantly change the energy required for the flame to survive. This behavior suggests the existence of a critical flame-kernel size required for self-sustained propagation, which is determined by the balance between chemical heat release and transport-induced losses. When the ignition radius increases beyond approximately 1.5 mm, the flame radius after ignition is sufficiently large that heat losses caused by diffusion no longer cause extinction. In this region, MIE_{prop} follows the cubic scaling trend ($E_{ig} \propto r_s^3$) and nearly coincides with the reference line.

The effect of ignition duration on MIE_{prop} was examined at two different ignition radii ($r_s = 1$ mm and $r_s = 2$ mm) to see whether a similar trend occurs. Results are shown in Fig. 9. Generally, a longer ignition duration allows more time for heat loss to the surrounding fresh mixture, reducing the net energy available to heat the ignition volume and modifying the temperature field. For a large ignition radius (here $r_s = 2$ mm), heat loss is mainly confined to a thin outer layer at the boundary of the ignition source, while the temperature at the center remains nearly unchanged, allowing ignition to occur; thus, MIE is weakly sensitive to ignition duration. In contrast, for a small ignition radius (here $r_s = 1$ mm), heat loss affects the entire kernel, including the center, leading to an overall temperature reduction and altered gradients. This significantly weakens reaction rates, making MIE strongly dependent on ignition duration.

A longer ignition duration allows more time for heat loss to the surrounding fresh mixture, resulting in a higher MIE_{prop}. In other words, as τ_s increases, the net energy available for heating the ignition volume decreases due to enhanced thermal diffusion, and thus a larger total ignition energy is required to achieve self-sustained flame propagation. In contrast, for larger ignition radii, the surface-to-volume ratio becomes smaller, reducing the relative importance of heat loss. Consequently, MIE_{prop} becomes nearly independent of ignition duration when r_s is sufficiently large. This result is consistent with the results of hydrogen ignition in [17,21].

In experiments, the MIE of R32/air mixtures ranges from several millijoules to several tens of joules (see, e.g., [9,12,22,23]). According to [12], variations in measurement setups, such as spark duration and spark gap, are the main reasons for the wide range of reported MIE values. This trend is consistent with the present simulation results, which show that the ignition radius has a strong influence on MIE_{prop}, and that the ignition duration τ_s may also affect MIE_{prop}, particularly at small r_s. As r_s increases from 1.0 to 10.0 mm, the ignition radius becomes ten times larger, and the corresponding ignition volume (and thus MIE_{prop}) increases by roughly three orders of magnitude.

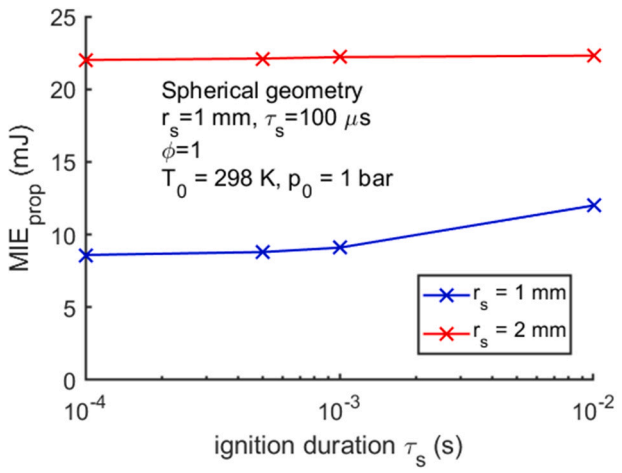

Fig. 9. Dependence of MIE_{prop} on ignition duration.

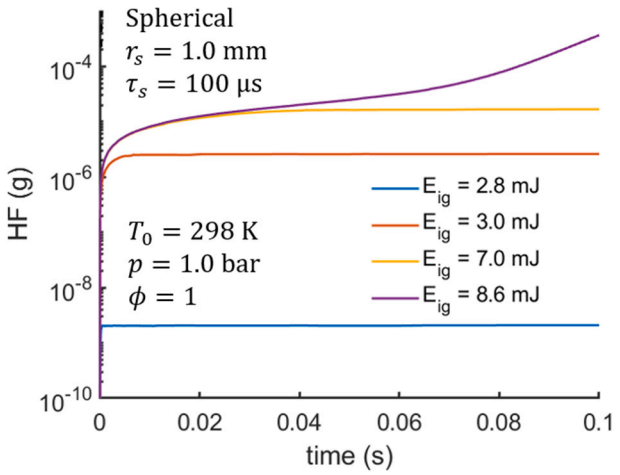

Fig. 10. Total amount of HF produced during the ignition and early flame propagation processes.

4.5. Total HF emission during the ignition and flame propagation of CH_2F_2/air mixtures

From an explosion hazard assessment perspective, our focus in the previous section lies on determining the minimum ignition energy, above which the flame can transition into a self-sustained propagation regime. However, from a process safety standpoint, it is of interest to examine the formation of toxic HF during the spark ignition process. Numerical simulations show that even at low temperatures, the production of toxic species such as HF can increase significantly over time. Therefore, it is necessary to investigate HF formation at different ignition energies, including cases of failed spark ignition.

For a complete reaction of a stoichiometric R32/air mixture, HF accounts for approximately 20% of the total mass, corresponding to about 2×10^5 ppm of HF in the flame kernel. Even in the case of flame extinction, a large amount of HF is generated within the flame kernel. This concentration is far above the EPRG-3 threshold of 50 ppm, which denotes the maximum safe one-hour exposure limit for toxic substances in air [24]. However, since the flame kernel remains very small during the early stage of flame propagation, the total amount of HF produced, rather than its local concentration, is the more relevant parameter for safety assessment.

Fig. 10 shows an example of total HF formation for a spherical geometry, $r_s = 1$ mm and $\tau_s = 10^{-4}$ s, with different ignition energies.

In the case of ignition failure, only trace amounts of HF are formed. When flame extinction occurs, HF formation stops as the flame quenches, and the total amount of HF generated depends strongly on the ignition energy. For example, at $E_{ig} = 7.0$ mJ, approximately 6 μg of HF is produced, corresponding to about 0.75 ppm in a 10 L volume, which is not considered critical. In contrast, during sustained flame propagation, HF is continuously generated. At $t = 0.1$ s, the HF concentration can reach approximately 50 ppm in the same 10 L volume.

It should be emphasized that, although flame extinction cases appear to be non-hazardous in the present configuration, the total amount of HF produced is strongly dependent on the ignition kernel size r_s, the spark duration τ_s, and the considered control volume. Under different geometrical or operational conditions, these parameters may vary significantly, leading to substantially different HF yields. In particular, even scenarios classified as flame extinction may result in non-negligible HF production if larger ignition volumes are considered. Therefore, HF formation in extinction regimes must be reassessed when applied to other practical configurations.

5. Conclusions

This study investigated the forced ignition, early flame development, and associated toxic HF formation in stoichiometric CH_2F_2/air mixtures using detailed one-dimensional numerical simulations. Emphasis was placed on the influence of ignition energy, ignition geometry, and curvature effects on the minimum ignition energy (MIE), flame evolution, and safety-relevant HF production.

A skeletal CH_2F_2 oxidation mechanism, derived from a previously optimized detailed model, was used to enable efficient one-dimensional simulations while preserving the key chemistry governing ignition, early flame propagation, and HF formation.

Three distinct ignition regimes were identified: ignition failure, flame extinction after kernel formation, and self-sustained flame propagation. The transition between these regimes is strongly governed by the competition between chemical heat release and diffusive losses, which is significantly affected by flame curvature during the early stage of flame growth. A minimum ignition energy for flame initiation (MIE_{ini}) and a minimum ignition energy for sustained propagation (MIE_{prop}) were defined, highlighting the existence of a transition regime where flame kernels form but cannot be sustained.

The results show that curvature effects play a critical role in determining flame stability at small flame radii. Strong curvature enhances diffusive transport, leading to increased heat and radical losses and potentially causing flame extinction even after successful ignition. As the flame expands, curvature decreases, and a transition from slow to fast propagation is observed once a critical kernel size is exceeded.

The MIE was found to depend on both ignition radius and ignition duration. For small ignition volumes, diffusive losses dominate and suppress flame growth, whereas for larger ignition radii the MIE scales approximately with the ignition volume. The ignition duration further influences MIE at small radii by modifying the balance between energy deposition and diffusive losses, while its effect becomes negligible for sufficiently large ignition volumes.

From a process safety perspective, HF formation was analyzed across all ignition regimes. Although local HF concentrations within the ignition kernel can become very high, the total HF amount is more relevant for hazard assessment. In the present configuration, critical HF production occurs only in the sustained flame regime (Scenario III), while ignition failure and flame extinction lead to smaller total amount of HF. However, this conclusion depends on the specific conditions considered here. Under different configurations, extinction cases may also produce critical amount of HF, and thus HF formation should be reassessed for other practical conditions.

Overall, the present work demonstrates that both explosion hazards and toxic product formation must be considered in a coupled manner when assessing ignition of CH_2F_2/air mixtures. The developed skeletal kinetic mechanism, together with the numerical framework, provides a reliable and computationally efficient tool for investigating ignition, flame propagation, and safety-relevant emission characteristics. The findings highlight the importance of ignition configuration in determining both MIE and toxic product formation. This is particularly relevant for fire scenarios in infrastructure systems, such as buildings and HVAC installations using R32, where leakage, confined geometries, and varying ignition conditions can strongly influence both flame development and toxic HF accumulation.

CRediT authorship contribution statement

Chunwei Wu: Writing – original draft, Visualization, Investigation, Formal analysis, Data curation. **Nafi Farzana:** Writing – review & editing, Visualization, Investigation, Data curation. **Heejeong Kim:** Investigation. **Bo Shu:** Writing – review & editing, Supervision, Funding acquisition, Formal analysis. **Ulrich Maas:** Writing – review & editing, Supervision, Methodology, Funding acquisition, Formal analysis, Data curation. **Chunkan Yu:** Writing – review & editing, Formal analysis, Data curation.

Declaration of competing interest

The authors declare that they have no known competing financial interests or personal relationships that could have appeared to influence the work reported in this paper.

Acknowledgments

The authors gratefully acknowledge the financial contribution from the Deutsche Forschungsgemeinschaft (DFG) under the project FOR 5507, project number 520588713.

Data availability

Data will be made available on request.

References

[1] Daikin Industries L. What's R-32?. 2024, https://www.daikin.com/air/daikin_techknowledge/benefits/r-32.
[2] Li J, Yang Z, He H, Zhang C, Hao S. Research on the flammability and explosion characteristics of typical low GWP refrigerants. J Loss Prev Proc 2022;80:104923.
[3] Mota-Babiloni A, Navarro-Esbrí J, Makhnatch P, Molés F. Refrigerant R32 as lower GWP working fluid in residential air conditioning systems in Europe and the USA. Renew Sustain Energy Rev 2017;80:1031–42.
[4] ISO817-2014. Refrigerants-designation and safety classification. 3rd ed.. International Organization for Standardization (ISO); 2014, p. 1–73.
[5] Zhang Y, Yang Z, Lv Z, Chen Y, He H, Chen S, Liu B. Research on the effect of flame retardants on the mildly flammable refrigerant ammonia. J Loss Prev Proc 2022;77:104787.
[6] Zhao Z, Luo J, Yang K, Zou D, Wang Q, Chen G. Experimental study on the influence of flame retardants on the flammability of R1234yf. J Loss Prev Proc 2023;81:104945.
[7] Hegetschweiler MJ, Pagliaro JL, Berger L, Hesse R, Beeckmann J, Bariki C, Pitsch H, Linteris GT. Data reduction considerations for spherical R-32 (CH2F2)-air flame experiments. Combust Flame 2022;237:111806.
[8] Imamura T, Sano T, Yuzawa K, Sugawa O. Experimental evaluation of the possibility of ignition and flame propagation in accumulated difluoromethane (R32) from a kerosene cigarette lighter. J Loss Prev Proc 2016;43:29–34.
[9] Takizawa K, Igarashi N, Tokuhashi K, Kondo S. Effects of temperature and pressure on quenching distances of difluoromethane (R32) and ammonia (R717). Sci Technol Built Environ 2018;24(1):97–104.
[10] Feng B, Yang Z, Zhai R. Experimental research on the concentration characteristics of R32 and R161 combustion product HF. Energy 2017;125:671–80.
[11] Burgess Jr. DR, Burrell RR, Babushok VI, Manion JA, Hegetschweiler MJ, Linteris GT. Burning velocities of R-32/O2/N2 mixtures: Experimental measurements and development of a validated detailed chemical kinetic model. Combust Flame 2022;236:111795.
[12] Askar E, Schröder V, Schmid T, Schwarze M. Explosion characteristics of mildly flammable refrigerants ignited with high-energy ignition sources in closed systems. Int J Refrig 2018;90:249–56.
[13] Farzana N, Glaznev R, Wang G, Agarwal S, Fernandes R, Beeckmann J, Shu B. Shock tube and laminar flame studies of CH2F2, CH4 and their blends with genetic algorithm-based mechanism optimization. J Fluor Chem 2025;110509.
[14] Babushok VI, Burgess DRJ, Kim DK, Hegetschweiler MJ, Linteris GT. Modeling of combustion of fluorine-containing refrigerants. Tech. rep., Gaithersburg, MD: National Institute of Standards and Technology (NIST); 2021.
[15] Mohamed AAE-S, Sahu AB, Panigrahy S, Baigmohammadi M, Bourque G, Curran H. The effect of the addition of nitrogen oxides on the oxidation of propane: An experimental and modeling study. Combust Flame 2022;245:112306.
[16] Hesse R, Glaznev R, Langer R, Schwenzer C, Babushok V, Linteris G, Pitsch H, Beeckmann J. Exploring nonlinear flame speed inhibition effects in mixtures of R1234yf and R32 under microgravity conditions. Proc Combust Inst 2024;40(1):105418.
[17] Maas U, Warnatz J. Ignition processes in hydrogen-oxygen mixtures. Combust Flame 1988;74(1):53–69.
[18] Maas U, Raffel B, Wolfrum J, Warnatz J. Observation and simulation of laser induced ignition processes in O2- O3 and H2- O2 mixtures. In: Symposium (international) on combustion. vol. 21, Elsevier; 1988, p. 1869–76.
[19] Wu C. Numerical studies on the induced ignition process of various fuels (Ph.D. thesis), Karlsruhe Insitute of Technology; 2024.
[20] Wu C, Chen Y-R, Schießl R, Shy SS, Maas U. Numerical and experimental studies on minimum ignition energies in primary reference fuel/air mixtures. Proc Combust Inst 2023;39(2):1987–96.
[21] Frendi A, Sibulkin M. Dependence of minimum ignition energy on ignition parameters. Combust Sci Technol 1990;73:395–413.
[22] Smith GP, Golden DM, Frenklach M, Moriarty NW, Eiteneer B, Goldenberg M, Bowman CT, Hanson RK, Song S, Gardiner WCJ, Lissianski VV, Qin Z. GRI-mech 3.0. 2000, http://combustion.berkeley.edu/gri-mech/version30/text30.html. [Accessed 22 July 2023].
[23] Sadaghiani MS, Arami-Niya A, Zhang D, Tsuji T, Tanaka Y, Seiki Y, May EF. Minimum ignition energies and laminar burning velocities of ammonia, HFO-1234yf, HFC-32 and their mixtures with carbon dioxide, HFC-125 and HFC-134a. J Hazard Mater 2021;407:124781.
[24] American Industrial Hygiene Association (AIHA). AIHA guideline foundation, ERPG/WEEL handbook. Falls Church, VA: American Industrial Hygiene Association; 2015.